Birefringence measurements on polymer melts in an axisymmetric flow cell

Rheol Acta (2002) 41: 114–133

ORIGINAL CONTRIBUTION

Birefringence measurements on polymer melts in an axisymmetric flow cell

Philip Harrison
Luc J. P. Janssen
Vincent P. Navez
Gerrit W. M. Peters
Frank P. T. Baaijens

Received: 2 April 2001
Accepted: 27 August 2001

P. Harrison · L. J. P. Janssen
G. W. M. Peters (✉) · F. P. T. Baaijens
Section of Materials Technology
Department of Mechanical Engineering
Eindhoven University of Technology
PO Box 513, 5600 MB Eindhoven
The Netherlands
e-mail: g.w.m.peters@tue.nl

V. P. Navez
NMC sa, Rovert 10, B-4731 Raeren
Belgium

Abstract The stress-optical rule relates birefringence to stress. Consequently, measurement of flow birefringence provides a non-intrusive technique of measuring stresses in complex flows. In this investigation we explore the use of an axisymmetric geometry to create a uniaxial elongational flow in polymer melts. In axisymmetric flows both birefringence and orientation angle change continuously along the path of the propagating light. The cumulative influence of the material's optical properties along the light's integrated path makes determination of local birefringence in the melt impossible. One can nevertheless use birefringence measurements to compare with predictions from computer simulations as a means of evaluating the constitutive equations for the stress. More specifically, in this investigation we compare the light intensity transmitted through the experimental set-up vs entry position, with the theoretically calculated transmitted intensity distribution as a means of comparing experiment and simulation. The main complication in our experiments is the use of a flow cell that necessarily consists of materials of different refractive indices. This introduces refraction and reflection effects that must be modeled before experimental results can be correctly interpreted. We describe how these effects are taken into account and test the accuracy of predictions against experiments. In addition, the high temperatures required to investigate polymer melts mean that a further complication is introduced by thermal stresses present in the flow cell glass. We describe how these thermal-stresses are also incorporated in the simulations. Finally, we present some preliminary results and evaluate the success of the overall method.

Key words Viscoelastic · Axisymmetric flow · Birefringence · Polymer melt

Introduction

A major goal of non-Newtonian fluid mechanics is to determine constitutive models for polymeric fluids that can accurately predict the stresses in flows of arbitrary kinematic complexity. The constitutive models can be used to simulate diverse fluid mechanical problems. Examples are found in industrial polymer forming and processing applications and also in bio-mechanics where the flow of viscoelastic fluids are involved in the body's mechanics. Furthermore, from a purely scientific perspective, the accuracy of these models can reveal clues regarding the fundamental nature of the molecular dynamics of polymeric materials. However, numerous constitutive models have been proposed and until the recent introduction of the "Pom-Pom" model (McLeish and Larson 1998; Verbeeten et al. 2001) no one model has proved superior to all the others in every flow

situation. An important final goal of this work, then, is to provide a stringent test of the most promising constitutive models for polymer melts. For that, both uniaxial and planar elongational flows are important. However, existing tension methods are restricted to relatively low strain rates and to elongational thickening materials. Neither of these restrictions applies to stagnation flows (Peters et al. 1999; Baaijens et al. 1994; Li et al. 2000) which are, in general, not homogeneous. In terms of testing constitutive equations, inhomogeneous flows are more demanding than homogeneous flows as they are transient by definition (from a material particle point of view) and they produce changes in flow kinematics that are otherwise difficult to achieve. The work presented here is concerned primarily with the experimental measurement of the stresses in a polymer melt in an axisymmetric geometry, generating locally a uniaxial elongational flow, using flow birefringence.

Flow birefringence is a useful non-invasive technique that can be employed to study transparent polymers. During flow, long polymer molecules are orientated by stresses in the fluid (Fuller 1995; Kroger et al. 1997). This molecular orientation results in a degree of structural and consequently optical anisotropy in the fluid. At a macroscopic level, the optical anisotropy can be expressed by the material's refractive index tensor. In many polymeric fluids a linear relationship, known as the stress-optical rule (SOR) (Lodge 1955), exists between the stresses in the fluid and its refractive index tensor. Thus, when light samples the polymer's refractive index tensor, it indirectly samples the material stresses. The SOR can be expressed as

$$\underline{n} = C\{\underline{\tau} + p\underline{I}\} + n\underline{I} \quad (1)$$

where $\underline{n}$ is the refractive index tensor, $\underline{\tau}$ is the extra-stress tensor, p is the hydrostatic pressure, $\underline{I}$ is the second-order unit tensor, C is the stress-optical coefficient, and n is the mean refractive index (Janeschitz-Kriegl 1983).

Since the final goal is to produce models that can predict stresses in flows of arbitrary kinematic complexity, the flow geometry should ideally explore as wide a range of complexity as possible. However, the computational requirements of simulating the flow field should be kept to a reasonable level. Most previous investigations have overcome this limitation by choosing approximately 2-D flow fields, but has its costs. It has a limited range of kinematic complexity and 3-D experimental end-effects at the viewing windows cause errors (Galante and Frattini 1991). The size of this latter type of error has recently been examined by Bogeards et al. (1999). Here we follow the example set by Li and Burghardt (1995) and employ an axisymmetric geometry that overcomes the need for 3-D viscoelastic analysis. In this geometry, uniaxial elongational flow can be generated which is the most strongly orientating flow and a severe test case for constitutive models.

In an axisymmetric flow the stresses and consequently the optical properties change continuously along the propagation path of the light beam. The two measured optical properties, retardance δ' and orientation angle χ', reflect the cumulative effect of the 3-D stress distribution on the polarization-state of the light. Integration along the light-beam's path maps three independent quantities: shear stress τ_{rx} and first and second normal stress differences $N_1(r,z) = \tau_{zz}(r,z)-\tau_{rr}(r,z)$, $N_2(r,z) = \tau_{rr}(r,z)-\tau_{\theta\theta}(r,z)$ respectively. These three quantities cannot be retrieved from the two experimentally accessible data. This reflects the main disadvantage of the use of birefringence in axisymmetric flow: if one has no a priori information of the stress distribution, direct conversion of δ' and χ' into stress components, through the stress optical rule, is not feasible. Rather than attempting to invert the optical data to yield the radial stress distribution, the optical property distribution serves as a basis for comparison with numerical simulations, as proposed by Li and Burghardt (1995). Because they are derived from simulated stress fields, the theoretically determined optical properties are highly sensitive to the choice of constitutive equation.

In their investigations on polymer solutions, Li and coworkers (Li et al. 1998, 1999, 2000; Li and Burghardt 1995) used refractive index-matched materials within the flow cell in order to prevent complications due to refraction of the sampling light beam. The fundamental difference with that work is that we model the effects of refraction on the laser light as it passes through the flow cell. In so doing, we remove the index-matching restriction and significantly extend the range of materials that can be investigated. Furthermore, once the effects of refraction are modeled it becomes possible to surround the flow-geometry with heated transparent silicon oil in order to investigate polymer melts at elevated temperatures. In this paper we describe the flow cell construction, the optical modeling required to interpret the results, and some preliminary comparisons between numerical and experimental results.

Experimental set-up

Extruder line and flow cell

The line-up of the most important units in the experimental set-up is schematically illustrated in Fig. 1. Details regarding the manufacturer and type of components can be found in Janssen (2000). A twin-screw extruder is used as a pump, with a gear-pump in line to prevent a fluctuating flow-rate. A by-pass is inserted between the extruder-nozzle and the gear pump to prevent pressure build up at low rotation speeds of the gear-pump. A static mixer containing four flow-diverting elements is used as a thermal equilibration zone.

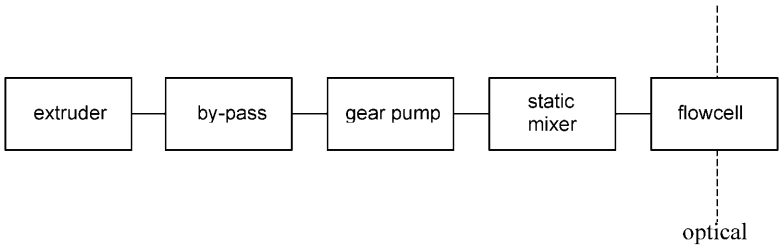

Fig. 1 Schematic of the experimental set-up: extruder, by-pass, gear-pump, static mixer, flow cell, and optical set-up

Finally, the melt is forced through the flow cell. A rail holding the optical components is placed perpendicular to the long-axis of the flow cell in order to make optical measurements.

The flow cell consists of an axisymmetric tube flow (inner diam. $D_2 = 1.5$ cm) past a centered, cylindrical obstruction ($D_1 = 0.75$ cm) with a hemispherical cap or "torpedo" (see Fig. 2). This creates a stagnation point on the center of the cap. The flow cell can be mounted to the static mixer with both ends, creating two different flow configurations. Far upstream or downstream of the stagnation point the flow is shearing. In the forward flow configuration (Fig. 2a) the flow exhibits biaxial extension in the neighborhood of the stagnation point. By reversing the flow direction (Fig. 2b), uniaxial extension is generated downstream of the stagnation point.

The flow cell has a transparent middle test-section made of optical glass (Schott, BK-7, see Table 1)

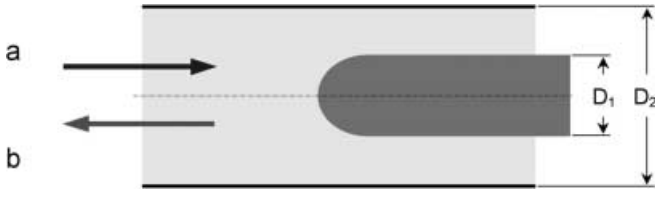

Fig. 2 Schematic of the test geometry: a cylindrical obstruction in an axisymmetric tube flow. The flow cell can be mounted to the static mixer with both ends, creating two different flow configurations: forward flow (a) and reversed flow (b). In this investigation the experiments are restricted to just the reversed flow configuration

consisting of an outer block (square cross section, 5×5 cm, with a cylindrical hole 4 cm diameter) and an inner tube (outer/inner diameter 3/1.5 cm) that is centered using Teflon rings. A square cross-section caused the laser beam to diverge while numerical simulations revealed that, with a cylindrical outer glass block, rays exiting the flow cell would converge and cross before diverging, severely complicating the final intensity pattern.

The test section is mounted between two steel end-blocks. The obstruction (steel, X14CrS17) is mounted in one of these end-blocks with three tangential leaf springs to ensure the correct position of the torpedo axis at high temperatures. The flow cell is heated by circulating externally heated silicone oil (DC 550, Dow Corning) in the gap between the outer block and the inner cylinder.

In order to minimize stresses in the glass, introduced by a difference in thermal expansivity of the glass test-section ($8.3 \times 10^{-6}\ K^{-1}$) and steel end blocks ($12 \times 10^{-6}\ K^{-1}$) (Callister 1997) these components are bonded by a 2 mm thick layer of heat-resistant silicone rubber which also prevents leakage of the silicone oil. The prescribed form and position tolerances are given in Fig. 3.

Optical set-up

The component numbers in this section refer to Fig. 4 and Table 2. A He-Ne laser (9) is used to create a monochromatic light-beam of wavelength $\lambda = 632.8$ nm

Table 1 Physical and optical properties of BK-7 glass. A summary of the most important physical and optical properties of BK-7 (Borosilicate Crowns) optical glass is listed in Table 1 (Schott 1998)

	Symbol	Value	Unit
Physical property			
Young's modulus	E	8.15×10^{10}	$N \cdot m^{-2}$
Density	ρ	2.51×10^{3}	$Kg \cdot m^{-3}$
Tensile strength	$ó_t$	60×10^{6}	$N \cdot m^{-2}$
Glass transition temperature	T_g	557	°C
Poisson's ratio	v_d	0.206	–
Coefficient of linear thermal expansion	$\alpha_{20/300}$	8.3×10^{-6}	K^{-1}
Thermal conductivity	k	1.114	$W \cdot m^{-1} \cdot K^{-1}$
Optical property			
Stress-optical coefficient (21 °C)	C	2.77×10^{-12}	$M^2 \cdot N^{-1}$
Index of refraction @ $\lambda = 632.8$ nm (170 °C)	n	1.51557	–

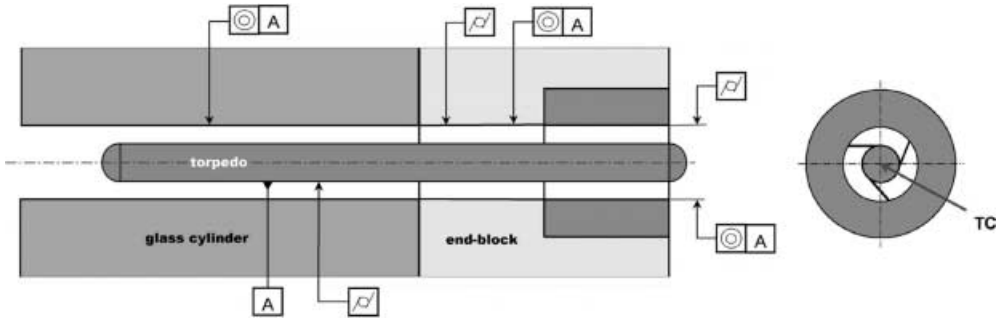

Fig. 3 *Left:* schematic of the prescribed form and position tolerances for the torpedo inside the flow cell; *right:* torpedo attached to the mounting ring in the thermal center (TC) by three tangential leaf springs

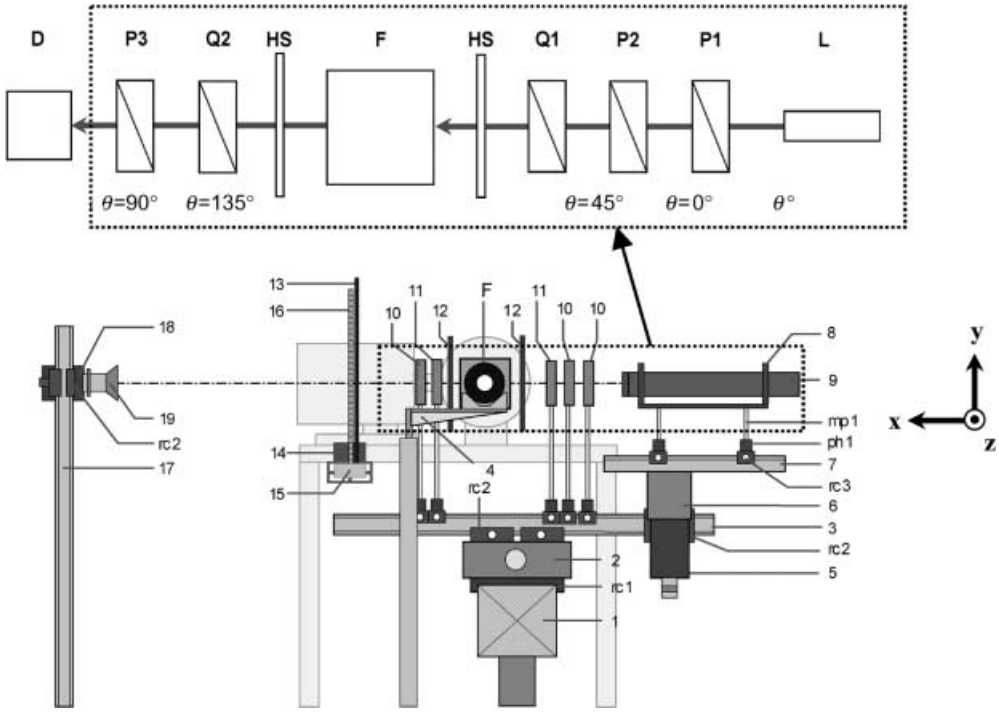

Fig. 4 Optical set-up and axis of the lab-frame. The optical components of the rail appearing inside the *dashed box* of Fig. 4 are shown in more detail in the insert. θ indicates the orientation angle of the optical elements in the *yz*-plane. The number between brackets denotes the component in the optical rail set-up (refer to Table 2 where the manufacturer and type of the optical components are listed)

and Gaussian width $D = 0.81$ mm. The light intensity of the exiting beam can be controlled, without interfering with the settings of the other optical components, by means of two linear dichroic polarizers (10). The first can be rotated about the *x*-axis, giving a variable orientation angle θ with respect to the *y*-axis. The second has a fixed transmission axis parallel to the *y*-axis ($\theta = 0°$), resulting in vertical polarized light. Third in line is a zero-order, quarter wave polymer retarder (11), oriented at $\theta = 45°$ to eliminate the presence of isoclines in the intensity results.

A protective heat shield (12) with vertical slit is placed between the heated flow cell and polymer retarder to keep the retarder's temperature within the correct operating range (−20 °C and +50 °C). The vertical slit (5 × 50 mm), enables off centerline (the horizontal symmetry line of the flow cell) measurements to be made. On exiting the retarder, the state of polarization is changed from vertical into left-circular polarized light[1].

The light-beam is then aimed through the flow cell and the exiting beam is incident on a second polymer retarder (11), oriented at $\theta = 135°$ and, next, a linear dichroic polarizer (10), oriented at $\theta = 90°$ (i.e., P2 and P3 have crossed transmission axis). Finally, the beam is projected on a translucent coated Perspex screen (13), and the image on the back of the screen is recorded.

The He-Ne laser (9) mounted on the top optical rail (7) can be vertically adjusted with a small translation stage (5) placed on the secondary optical rail (7). The optical components also mounted to this secondary optical rail can move in the flow cell's axial direction

[1]The handedness of the circularly polarized beam is determined by observing the rotation direction of the electric field vector when looking back at the light source.

Table 2 Component function, item, manufacturer, type and number of the optical rail

No.	Function	Item	Manufacturer	Type	#
Base					
1	Primary optical rail	Optical rail	Newport	–	1
rc 1	Rail carrier	Rail carrier	Newport	CX95AS	2
2	Translation stage for axial positioning secondary optical rail	Translation stage	Cleveland	SM14	1
rc 2	Rail carrier	Rail carrier	Newport	M-CX48–80	2
3	Secondary optical rail	Optical rail	Newport	–	1
4	Flow-cell support	Flow-cell support	Mate	–	1
Top optical rail					
rc 2	Rail carrier	Rail carrier	Newport	M-CXL48–80	1
5	Vertical adjustment of the top optical rail	Translation stage	Cleveland	s = 50 mm	1
6	Mounting frame for top optical rail	Mounting frame	Mate	–	1
7	Top optical rail	Optical rail	Melles Griot	07-ORN-005	1
Laser and optical elements					
rc 3	Rail carrier	Rail carrier	Melles Griot	07-OCN-501	6
ph 1	Post holder	Post holder	Melles Griot	07-PHS-001	6
mp 1	Mounting post	Mounting post	Melles Griot	07-RMS-003	6
8	Laser mounting platform	Laser mounting platform	Melles Griot	–	1
9	HeNe Laser (illumination beam)	HeNe Laser	Uniphase	1125P, λ = 632.8 nm P = 10 mW	1
10	Polarizer	Linear dichroic polarizer	Meadowlark Optics	DPM-200-VIS1	3
11	Retarder	Quarter wave polymer retarder	Meadowlark Optics	PQM-	2
12	Minimize heat radiation from flow-cell	Heat shield	Mate	–	2
F	Flow-cell	Flow-cell	Mate	–	1
Projection screen/camera					
13	Focal plane for camera	Perspex projection screen	–	–	1
14	Frame mounting	frame mounting	Mate	–	2
15	Optical rail	optical rail	Melles Griot	–	1
16	Determination vertical position	ruler	–	–	1
17	Vertical displacement camera	optical rail	Newport		1
rc 2	Rail carrier	Melles Griot	Newport	M-CXL48–80	1
18	Analogue camera	analogue camera	Pulnix	TM-765	1
19	Zoom lens	zoom lens	Canon	18–108 mm (1:2,5)	1
–	Frame grabbing and image storage	computer	–	–	1

(z-axis) with translation stage (2). This allows for measurements in the entire test section of the flow cell. A metal ruler (16) is attached to the projection screen (recording side) for determination of the vertical intensity pattern position. To reduce noise from ambient room light, the experimental area is enclosed with black curtains. An analogue CCD camera, 571×763 pixels, 256 gray values (18), is used to record images of the intensity pattern. The non-linearity of the camera's recorded gray value vs intensity was determined using two linear polarizers to vary the light intensity. All subsequent data were modified to account for this non-linearity.

Optical modeling

The laser beam passes through various constituent components in the test section (glass components, oil, and polymer melt) with different refractive indices and,

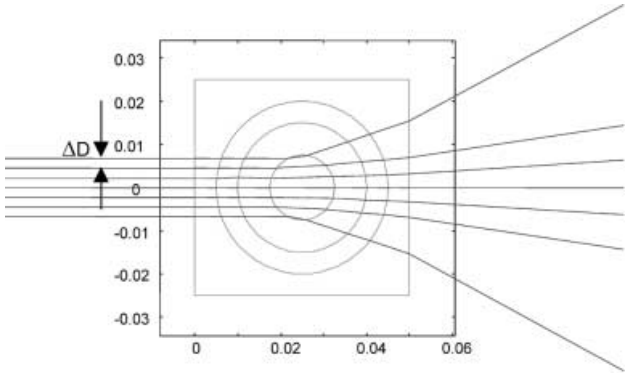

Fig. 5 The diagram shows seven rays passing through the flow cell. The distance between the equally spaced rays is denoted by ΔD. The refractive index used in this example are: $n_{air} = 1.0$, $n_{glass} = 1.51557$, $n_{oil} = 1.4935$, and $n_{polymer} = 1.423$

consequently, through various material-interfaces where it will undergo both refraction and partial reflection. A further factor to consider is diffuse scattering and absorption. As the polarization-state of the light exiting the flow cell depends explicitly on the stresses along its integrated path, it is vital to predict this path before any calculation of the transmitted light's polarization-state can be made. Furthermore, partial reflection of the light at the interfaces can also change the polarization-state of the propagating beam. A computer code (Harrison 2000) has been written to model all these effects. Thus, the physical influences included in the code are refraction, reflection, diffuse scattering, absorption, and also the birefringence of the materials. Here we outline how these influences affect the laser light and briefly describe how they are modeled. Selected results produced by the code are presented and discussed.

Refraction

The laser beam traverses material interfaces that are non-perpendicular to the propagation direction, $\bar{k}$. At these interfaces the propagation direction of the light is altered. The resultant effect of the interfaces is to deflect the beam either up- or downwards in a plane lying perpendicular to the long axis of the cylindrical tube (the z-axis referring to Fig. 4) and to spread the beam out into a vertically orientated, diverging light sheet. The divergence means that the intensity must decrease with increasing distance from the flow cell.

In our model, the finite width of the laser beam was approximated by a given number of initially parallel, equally spaced rays. Throughout this analysis we distinguish between a 'ray' as being a mathematical line of zero thickness and a 'beam' as being a physical stream of light of finite width. When using the code, the Gaussian-width of the beam, the number of rays, and the height at which the central ray hits the flow cell are specified by the user. The path of each ray through the flow cell is calculated using a combination of Snell's law and trigonometrical calculation; see for example Fig. 5.

The details of the calculations can be found in Harrison (2000). The divergence of the beam was used in calculating the decrease in intensity of light along a given path (see Fig. 6).

Fig. 6 The *left* diagram shows seven rays passing through the flow cell (plus a retarder, a polarizer, and the Perspex screen). ΔY_1 is the distance between the first and second rays at the screen while ΔY_2 is the distance between the second and third rays at the screen. The ratio between ΔD and ΔY_1 and ΔY_2 is used to approximate the decrease in intensity of the second ray from the top, i.e., the decrease in intensity of the second ray from the top is approximated by the value Q, where $Q = 0.5\Delta D[1/(\Delta Y_1 + \Delta Y_2)]$. Using this method the decrease in intensity of each ray, due to beam spreading, vs ray number, is shown in the diagram to the *right* (101 rays were used for this particular simulation in order to create a smoother curve)

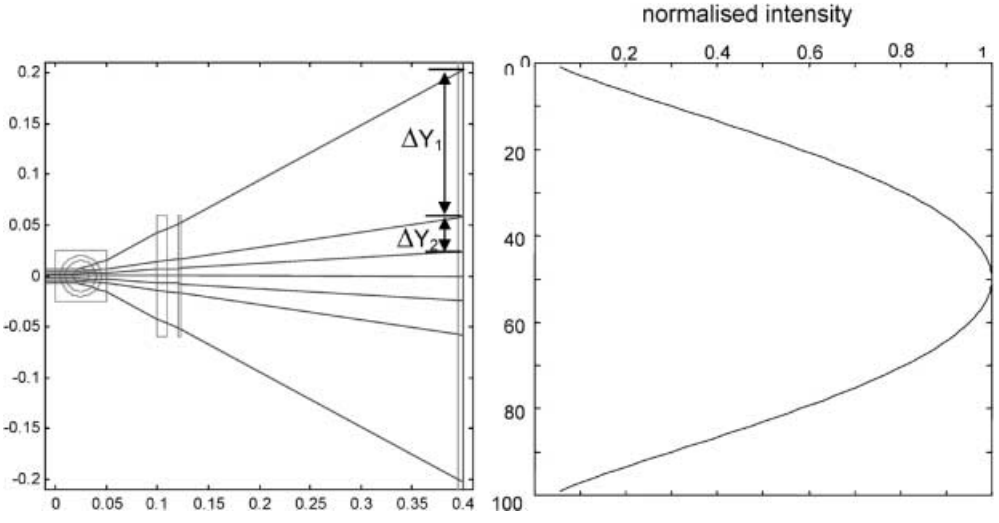

In this example, at the edges of the beam the normalized intensity has been reduced to around 10% of the beam's central intensity. The intensity distribution of Fig. 6 is due only to the spreading of the beam; the Gaussian intensity distribution of the laser beam is not included in this example.

Partial reflection

As light passes through an interface it is both partially reflected and partially transmitted. The transmitted proportion depends primarily on three factors: the ratio between the refractive indices of the two materials, the ray angle between the propagation direction and the surface normal, and the polarization-state of the light. Unequal transmittance of different polarization-states at non-orthogonal interfaces means that the polarization-state of light can be altered on passing through an interface. The polarization-state of light exiting the flow cell, will depend on both the height at which the laser enters the flow cell and the polarization state of the light whilst traversing the interface.

Partial reflection of light at each interface has been incorporated in the code using Fresnels' equations. These equations predict the change in amplitude, and consequently the decrease in transmitted intensity, of two types of polarized light on traversing an interface. These two polarization states are known as transverse electric and transverse magnetic light (Pedrotti and Pedrotti 1987). In our experiments they correspond to horizontally (H) and vertically (V) polarized light respectively. Any other polarization state, such as circularly polarized light (C), can be expressed as a combination of these two states using Jones vector calculus (see, for example, Hecht 1998). Jones vector calculus is based on the amplitude of the light's electric vector. Figure 7 shows the light intensity transmitted through the flow cell, of three differently polarized laser beams vs their distances from the centerline on arrival at the screen. These states include V, H, and C polarized light. The intensity distribution due to spreading of the rays is not included in this figure.

A few points regarding Fig. 7 are noted. The H-light behaves as one might expect and its intensity decreases as the beam moves away from the centerline because more of the light is reflected as it passes through the increasingly non-orthogonal interfaces. However, perhaps counter-intuitively, the transmitted intensity of V-light is actually seen to increase as the rays move further away from the centerline. This is true only for relatively small angles of incidence and as this angle increases towards the critical angle of total reflection, the intensity begins to decrease. Because C-light is composed of equal amounts of V- and H-light this effectively means that the polarization-state of C-light is altered on propagating through a non-orthogonal interface and the transmitted light is no longer in a C-state when leaving the flow cell, even in the absence of birefringence. The original C-state becomes elliptically polarized with a progressively larger bias towards a V-state. Note however that the partial transmission of the light plays no part in changing the relative phase of the V and H components of the light and affects just their amplitudes.

Finally, we draw attention to the vertical scale in Fig. 7. The intensity distribution due to partial reflection at the interfaces is seen to be much less important than the distribution caused by the divergence of the beam (Fig. 6b) or indeed of the Gaussian distribution of the laser beam. In the Appendix we detail how Fresnels'

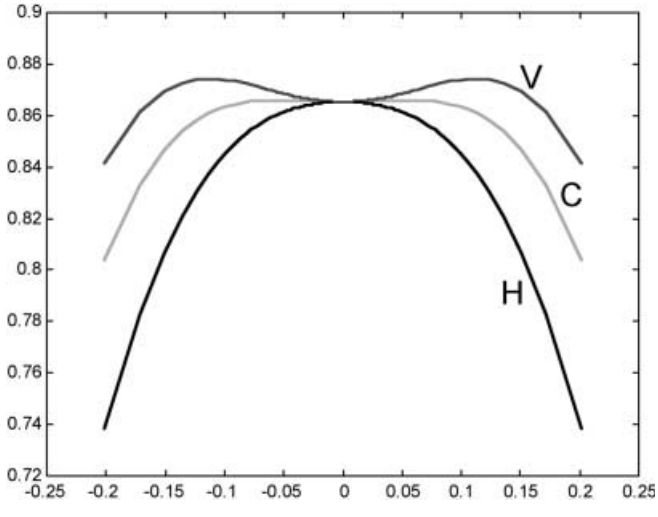

Fig. 7 Fraction of original light intensity transmitted through the flow cell (vertical axis) vs distance of rays from centerline at screen (cm). The *upper line* corresponds to V-light, the *lower line* to H-light and the *line in between* to C-light (see text for an explanation). The same refractive indices and beam width as in Figs. 5 and 6 were used

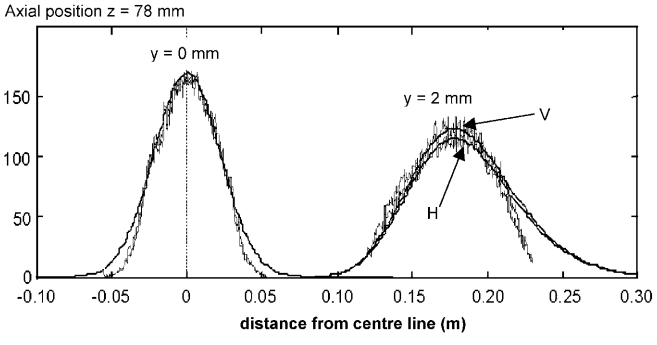

Fig. 8 Comparison between the Fresnel predictions and experiments. The distance between the screen and the nearest surface of the flow cell is 35 cm. The figure shows that on the centerline there is no noticeable difference between the intensity of the V and H polarized light transmitted through the flow cell. There is a noticeable difference between the transmitted intensity of the V and H polarized light off the centerline. This difference is predicted correctly by the computer code

equations have been employed to calculate the transmitted intensity. The influence of the unequal transmission of the V and H states can be clearly seen experimentally and is shown in Fig. 8. In these experiments the central core of the flow cell contained air rather than polymer melt. Predictions made using Fresnels' equations are also plotted in Fig. 8 and are seen to compare very well with the experimental data.

Diffuse scattering and light absorption

As the laser beam propagates through the flow cell, the laser light is visible in both the silicon oil and polymer melt but invisible in the glass components. This suggests that there is a significant amount of diffuse scattering in these two fluids (much more so than in the optical-glass, as one might expect). The amount of scattered light is highest in the polymer melt. This must be related to the length of the light path. While the path-lengths change considerably in the polymer melt (as a function of the rays entrance height), the path-lengths in the silicon oil are comparatively constant (Fig. 9).

Thus the polymer melt will play a much more significant role in changing the form of the intensity vs entry position distribution curve. For this reason, only the scattering and absorption of the polymer melt is included in the model. The transmitted intensity is related to path length through

$$I_t = I_o e^{-\alpha L} \tag{2}$$

where I_t is the transmitted intensity, I_o is the original intensity, α is the attenuation constant, and L is the path-length in the material. A typical result is shown in Fig. 10. Taking $\alpha = 100$ means that almost 80% of the light is lost along the centerline to absorption and scattering.

The optical modeling of the refraction, beam spreading, and scattering-absorption predictions have been compared against experiments. The results are shown in Fig. 11 and were produced with polymer melt (170 °C) at rest inside the flow cell with circularly polarized light entering the flow cell and with the analyzer removed from the experimental set-up. The laser beam is directed through the flow cell at progressively increasing heights above the centerline. The value of the refractive index of the polymer melt was adjusted to give the correct position for the various intensity distributions on the screen. This fixed the ray paths in the flow cell and effectively fixed the intensity distributions due to beam spreading (Fig. 6) and partial reflection at the interfaces (Fig. 7). These two distributions are multiplied together to produce a combined spreading-reflection distribution. This distribution is then multiplied by the absorption/scattering distribution (Fig. 10) to give the final intensity envelope. The value of the scattering-absorption attenuation constant, α, is determined by comparing the

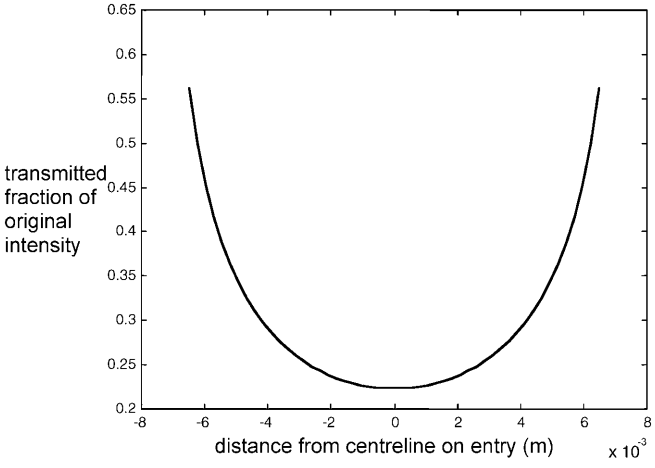

Fig. 10 Using an attenuation constant (α) of 100 produces a sensitive relationship between entry position and transmitted intensity. Along the centerline less than a quarter of the original laser energy is transmitted. This fraction will increase to 1 as the path length in the polymer approaches 0 m

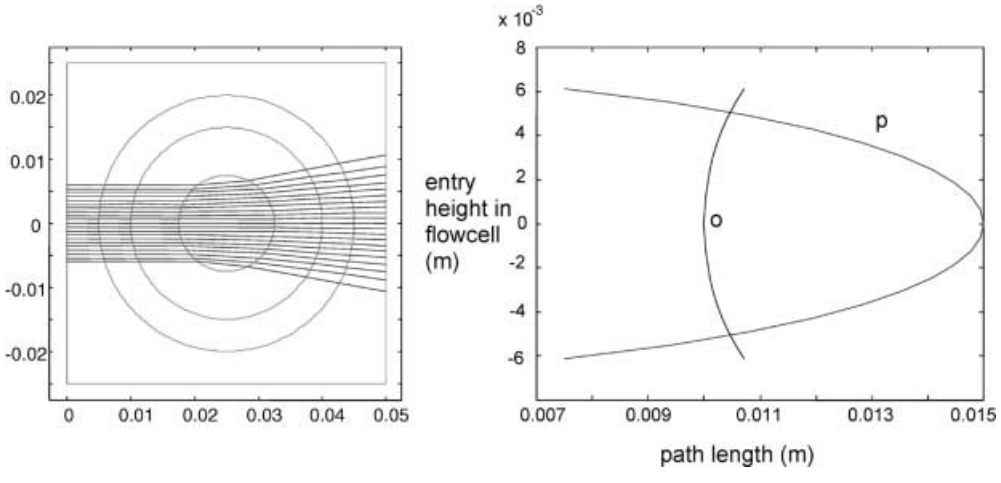

Fig. 9 *Left*: simulation of rays passing through the flow cell. *Right*: height at which rays enter flow cell vs path-length of rays in polymer (p) and the sum of both the oil-sections (o). The path-length in the polymer is seen to be much more sensitive to its entry position in the flow cell than that of the oil's path-length

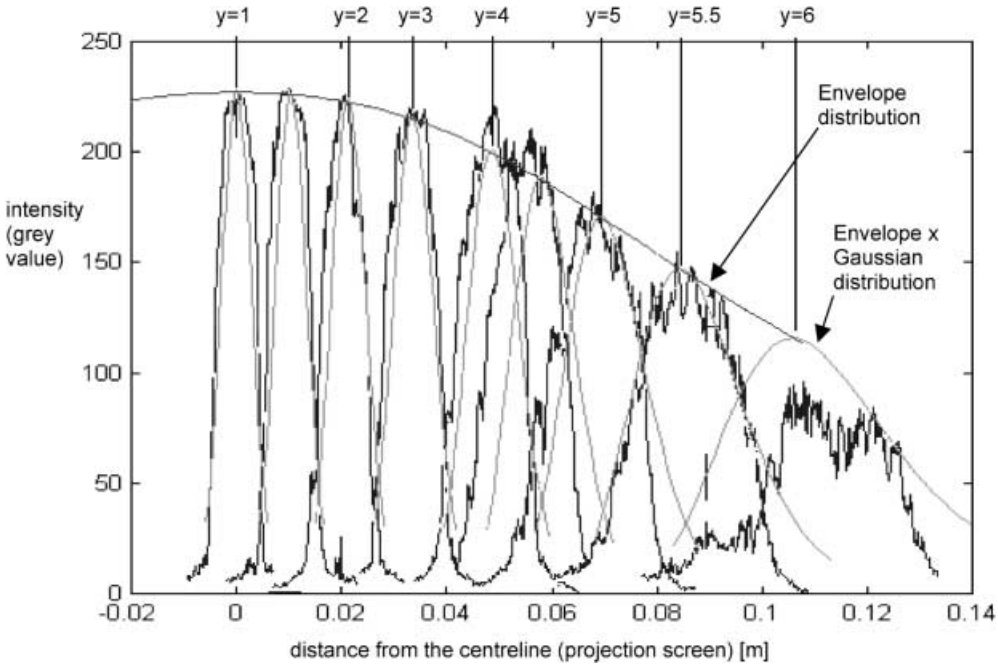

Fig. 11 Refraction experiment to fit the decrease in the beam's intensity due to absorption and scattering of the beam. The y position at the top of the figure indicates the distance of the center of the beam from the centerline. The refractive index, used for the polymer in order to fit the horizontal position of the simulation curves, is $n = 1.423$, the attenuation constant is $\alpha = 100$

difference between the predicted and measured transmitted intensity along the centerline, both with and without the polymer core. In the absence of scattering and absorption, the predicted intensity should increase with the introduction of the polymer core by approximately seven times, due to the decrease in beam spreading. However, the measured increase was much less than this. The difference between the predicted and observed change in intensity was used to estimate the size of α.

In Fig. 11 both the overall intensity-envelope, calculated from the Fresnel, spreading and scattering-absorption intensity envelopes, along with the Gaussian intensity distributions of the individual laser beams are included. The comparison shows that the simulations predict both the intensity and position of the image, to a high degree of accuracy, for all but the final intensity distribution ($y = 6$ mm). This is most likely due to a small imperfection, such as a scratch, on one of the interface. Scratches have since been removed by repeated polishing all of the glass surfaces of the flow cell.

Component material birefringence

During the flow of the polymer melt, every component of the flow cell is subject to some kind of stress field. The outer glass block is subject to thermal-induced stresses, the silicon oil and the polymer are both subject to flow-induced stresses, and the inner glass tube is subject to both pressure-induced stresses and shear stresses on its inner wall due to the flowing polymer. The stress-optic rule (Eq. 1) therefore implies that all of these materials are birefringent to some degree or another. In fact only the birefringence of the silicon oil is considered negligible in these optical simulations.

The total change in the polarization-state of the light, resulting from material birefringence, depends on both the magnitude of the material's birefringence and the direction and length of the light path in the material. As a result, changes in the intensity due to material birefringence will depend largely on two factors: the stresses in the flow cell glass and polymer melt and the height at which the light enters the flow cell.

Following each interface the polarization-state pertaining to a particular ray is calculated using Fresnels' equations, and recorded by its Jones vector (Hecht 1998; Azzam and Bashara 1992), as described in the Appendix. This Jones vector describes the polarization-state of the ray on passing through an interface and entering the following material. If this material happens to be the outer glass block, the inner glass tube, or the polymer core, then the polarization-state of the ray will be altered as it propagates through the material. In the Appendix we describe how we express the material anisotropy in the so-called kDB reference frame, before using Jones. Once this is done, the intensity distribution, due to the combined effect of the material's birefringence and the modulation of the final polarizer, is multiplied by the reflection-spreading-scattering-absorption intensity envelope (see Fig. 11) to give the final intensity distribution arriving at the translucent screen. In this manner we can compare experimental results with simulations and consequently test the validity of the stress fields used in the simulations.

It is worth noting here that expressing material anisotropy in the kDB system means that we calculate

the influence of the impermittivity tensor on the displacement vector of the propagating electromagnetic wave (Fuller 1995). A simpler but less accurate method of predicting the effect of the material anisotropy on the propagating light is to calculate the influence of the permittivity tensor on the wave's electric vector (see, for example, Li and Burghardt 1995). The inaccuracy in this second method is due to the slightly inaccurate assumption that in anisotropic materials the wave's electric vector is orthogonal to the propagation vector of the wave. Thus, the question is whether this inaccuracy is of significance when comparing results from flow birefringence experiments with simulations calculated using this simpler method. Calculations performed by both methods in this investigation showed that when incorporating stresses of realistic magnitude in the code, the difference is indeed negligible.

If the SOR remained valid for stresses of unlimited magnitude then one would expect to see increasing differences between results produced by the two methods as one used stresses of increasing magnitude (because of the material's increasing birefringence). This was indeed found to be the case in results of simulation. However, the stresses required to produce a noticeable difference in the results were so high that in reality one would expect the flow cell to break long before these kinds of stresses are reached. Therefore, it seems that unless the laser light propagates through a large thickness of highly stressed polymer then, for all intents, one can safely use the permittivity rather than the impermittivity tensor in the calculations.

Material characterization

The polymer melt investigated is a low-density polyethylene of type DSM Stamylan LD 2008 XC43. The most important material properties are listed in Tables 3, 4, and 5. A complete rheological characterization of the polymer melt is presented in Schoonen et al. (1998).

Calculation of stress fields

In order to predict the birefringence of each component inside the flow cell's transparent test section (glass components + polymer melt) the stresses within the various components have to be calculated. The following methods are used:

- The thermal stress field in the outer glass block is calculated using MARC, a commercial finite-element simulation program.
- The birefringence of the inner glass tube is approximated using the stress field derived for a cylindrical tube containing a fluid under pressure.
- The stress field in the polymer melt is calculated using POLYFLOW, a commercial finite-element program for simulating viscoelastic fluid flow.

Outer glass block: results from MARC simulations

The origin of the stresses in the outer glass block is the thermal gradient between the inside, which is heated to 170 °C, and the outside, which is cooled through convection by the surrounding air. The stresses are calculated by conducting two de-coupled finite-element simulations. The first simulation is a thermal analysis that provides the temperature field throughout the flow cell. The second simulation uses this temperature field as an initial condition and predicts the thermal-induced stresses within the glass block. Example results, showing a temperature and stress-field inside the outer glass block, are shown in Fig. 12.

In a zone of about ± 2.5 cm from the midsection, the thermal-induced stresses in the outer glass block are almost independent of the z-coordinate. Thus, the stress field half way along the length of the glass block can be used as a good approximation of the stress field present throughout the central region of the glass block. The boundary conditions on the outside of the glass block are not well defined. In particular, the

Table 4 Thermal properties of LDPE

Heat capacity	Thermal conductivity
$c_p = 2600$ (J/kg K)	$k = 0.22$ (W/mK)

Table 5 Optical properties of LDPE

Average stress optical coefficient	Refractive index gradient
$\overline{C} = 1.47 \cdot 10^{-9} \left[\frac{m^2}{N}\right]$	$\frac{\partial n}{\partial T} = -3.3 \cdot 10^{-4} [K^{-1}]$

Table 3 Material properties of the investigated LDPE melt. The melt index denotes the flowability of the batch, *Mn*: number average molecular weight, *Mw*: weight-average molecular weight, *Mz*: z-averaged molecular weight, *Tc:* crystallization temperature, ρ*:* density

Manufacturer	Grade	Melt index (dg/min)	Mn	Mw	Mz	T_c (°C)	ρ (kg/m^3)
DSM	Stamylan LD 2008 XC43	8	13,000	155,000	780,000	98.6	920

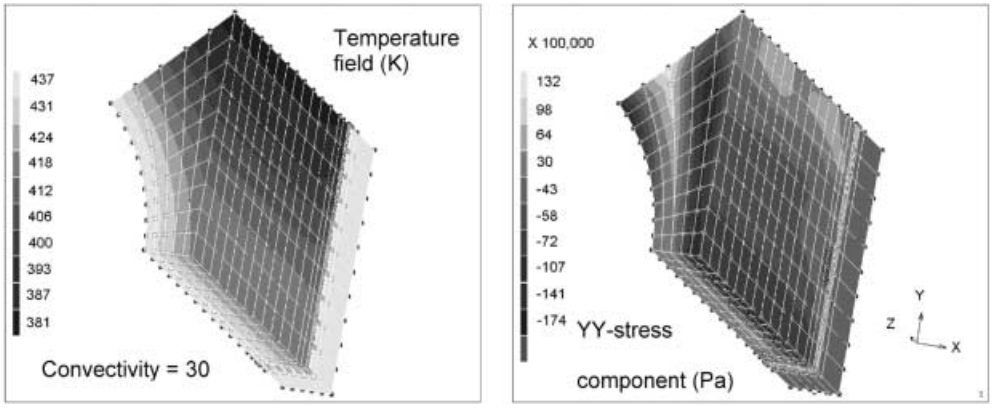

Fig. 12 Typical 3-D simulation result using MARC; note that because of the flow cell's symmetry only one-sixteenth of the flow cell is modeled. *Left*: thermal simulation; the convectivity coefficient was 30 and room temperature was taken as 293 K. *Right*: stress-simulation showing *yy*-stress component. The material properties used in the simulations are given in Table 1

convectivity-coefficient (H) is known only to lie somewhere in the range of 1–25 (Cengel and Boles 1994). The only way to determine H is through experimental tests as it is not a property of the glass itself but depends on numerous variables, including factors such as the geometry of the cooling body and the presence of drafts and humidity in the air. In order to account for this uncertainty, thermal simulations have been conducted using H ranging from 1 to 30. H is determined by comparing the measured light intensity passing through the heated flow cell (placed between crossed polarizers) when there is no flow. Figure 13 shows the transmitted intensity as a function of entry position. The intensity is normalized with respect to the maximum intensity that can be transmitted through the optical train. This intensity is found by removing the second polarizer. We determined H to be about 22 by fitting the theoretical curve to the experimental data. Each data point is taken as the maximum of the intensity distribution of the refracted beam. In so doing, the Gaussian distribution approximation of the laser beam intensity distribution (see, for example, Fig. 11) is not included in the data. The fit of the theoretical curve to the data is good near the centerline but tends to diverge from the experimental data when moving further than 4 mm away from the centerline. We believe this error is due to the angle at which the refracted light propagates through the second retarder; thus the experimental error becomes progressively larger for birefringence measurements taken further than 4 mm from the centerline. Figure 13 also shows the envelope of maximum possible intensity calculated both with and without scattering and absorption. The theoretical curve gives a much closer fit to the experimental data when including the scattering-absorption effects. The figure illustrates the importance of accounting for scattering and absorption in the modeling and also indicates the degree of accuracy of the experimental data.

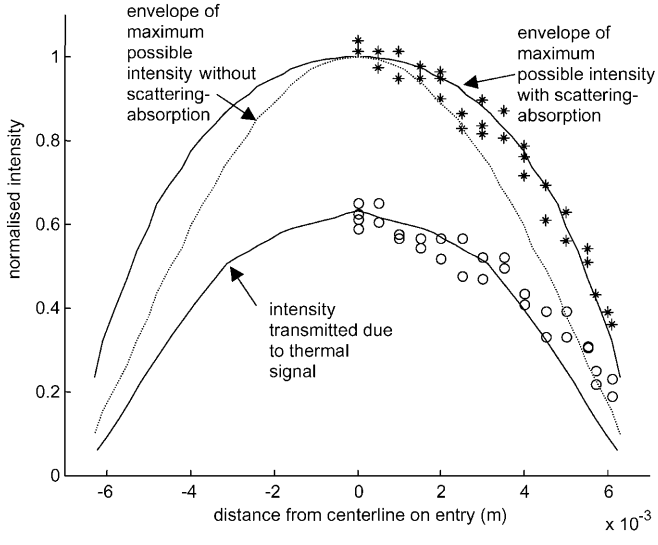

Fig. 13 Thermal birefringence measurements at 170 °C. The transmitted intensities are plotted vs their distances from the centerline when entering the flow cell. The intensity is normalized with respect to the maximum intensity passing through the centerline when the second polarizer is removed. The *circles* are experimentally measured data and the *lower continuous line* is fitted to the data by varying the convectivity coefficient in the FE simulations. The *upper continuous line* is the envelope of the maximum possible transmitted intensity when including diffusion effects in the calculation. The *dashed line* is the envelope of the maximum possible transmitted intensity calculated without diffusion effects

The stresses along the light paths of the different rays in the glass block are determined using a computer code (Harrison 2000). To do this the coordinates of the nodes and their corresponding stresses are copied from a MARC simulation into the code. Bilinear shape-functions are then used to interpolate between the nodes to a given xy-position. Figure 14 shows an example of three rays propagating through the glass block. Each ray is discretized along its length and the stresses calculated at the midpoint of each line segment are used to calculate the Jones matrix of the element (as discussed in the Appendix).

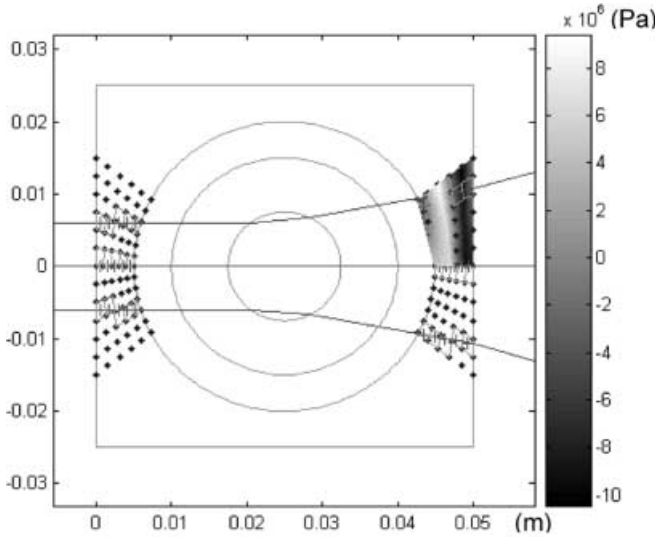

Fig. 14 Simulation showing three rays passing through the flow cell. The nodal positions and stress-components are copied from the MARC simulations. Only the relevant part of the block is modeled. Each ray is discretized into five elements as it propagates through the front and back walls of the outer glass block; a *cross* indicates the position used to calculate the stresses for each element. A Delaunay-triangulation method has been used to visualize the *yy*-component of the stress field in the top-right quarter of this figure, the legend is given on the right

Inner glass tube

We approximate the stresses in the inner glass tube using the analytical solution shown in Eqs. (3), (4), (5), and (6) (Ugural and Fenster 1995):

$$\tau_{rr}(r) = p \cdot \left\{ \frac{R_{inner}^2}{R_{outer}^2 - R_{inner}^2} \right\} \cdot \left\{ \frac{R_{outer}^2}{r} - 1 \right\}, \tag{3}$$

$$\tau_{\theta\theta}(r) = p \cdot \left\{ \frac{R_{inner}^2}{R_{outer}^2 - R_{inner}^2} \right\} \cdot \left\{ \frac{R_{outer}^2}{r} + 1 \right\}, \tag{4}$$

$$\tau_{r\theta}(r) = p \cdot \left\{ \frac{R_{inner}^2}{R_{outer}^2 - R_{inner}^2} \right\} \cdot \left\{ \frac{R_{outer}^2}{r^2} \right\} = 0 \text{ for no torsion} \tag{5}$$

$$\tau_{zz} = 0 \tag{6}$$

where R_{outer} is the outer radius of the tube, R_{inner} is the inner radius, r is the radial co-ordinate, z the axial direction, and p is the pressure which is provided by the polymer flow simulations. Because normal stresses in the glass are much greater than flow-induced shear stresses of the polymer and oil, we neglect these stresses in the calculations. The transform equations to convert the stresses from a cylindrical to a Cartesian system are given in the Appendix. As for the outer glass block, the ray path is discretized along its length. The stresses for each segment are calculated by first determining the stresses at the start and end of the segment. These stresses are averaged and then used to represent the stress of the element and produce the Jones matrix.

Numerical flow simulations

A commercial finite-element program, POLYFLOW, is used to calculate the stresses in the flowing polymer. Initially, several numerical methods, incorporating both integral and differential-type rheological models, were employed in attempts to simulate the flow. However, all numerical methods failed when reaching flow rates approximately half that of the minimum volumetric flow rate used in the experiments. However, as we wanted to make at least a qualitative comparison at this stage of the work, de-coupled simulations have been performed to calculate an approximate stress field (Debae et al. 1994; Douven et al. 1995; Baaijens et al. 1995). By this we mean that the velocity field is first calculated using a generalized Newtonian model, the Carreau-Yassuda model, for the viscosity, $\eta = \eta_o\left(1 + \left(\lambda\sqrt{|II_{\mathrm{D}}|}\right)^{\mathrm{a}}\right)^{(\mathrm{n}-1)/\mathrm{a}}$ where $|II_{2\mathrm{D}}|$ is the absolute value of the second invariant of the rate of deformation tensor and λ, a, and n are three further fitting parameters. The resulting velocity field is then used to calculate the stress field, using a post-processor incorporating a modified form of the K-BKZ model (Kaye 1962; Bernstein et al. 1963) proposed by Wagner (1976, 1977) and Wagner et al. (1979) (Eqs. 7, 8, 9, and 10):

$$\tau(t) = \int_{-\infty}^{t} m(t-t')h(I_1(t,t'), I_2(t,t'))C_t^{-1}(t')\mathrm{d}t' \tag{7}$$

$$m(t-t') = \sum_{i=1}^{N} \frac{G_i}{\lambda_i} e^{\frac{t-t'}{\lambda_i}} \tag{8}$$

$$h(I_1, I_2) = ae^{-n_1\sqrt{J-3}} + (1-a)e^{-n_2\sqrt{J-3}} \tag{9}$$

$$J = \beta I_1 + (1-\beta)I_2 \tag{10}$$

in which τ is the extra stress tensor, t is the present time at which the stress is evaluated, t' is some time in the past, $m(t-t')$ is the memory function, I_1 and I_2 are the first and second invariants of the relative Finger strain tensor, $C_t^{-1}(t')$, and $h(I_1(t,t'),I_2(t,t'))$ is the nonlinearity function. The parameters a, n_1, and n_2 are fitted on the nonlinear behavior in shear and β is fitted to elongational data. To satisfy the irreversibility condition (Wagner et al. 1979) used in these simulations, h should meet:

$$h(t,t') = \text{minimum}\, h(t'',t'), \quad t' \le t'' \le t \tag{11}$$

The Carreau-Yassuda model is fitted to data found in the literature (Schoonen 1998; Tas 1994) using a least-squares method. The parameter values of the modified K-BKZ model are taken from Tas (1994). Parameter values of both models and the Maxwell modes used in the simulations are given in Tables 6, 7, and 8. The finite-element mesh, close to the end of the torpedo, along with a pictorial example of the τ_{zz} component of the stress field, calculated at the highest flow-rate used in the experiments, is shown in Fig. 15.

Discussion of flow-experiment results

Before trying to evaluate the performance of the rheological model it is useful to consider what information, in principle, can be understood from the results. In this preliminary investigation we have used an optical train designed to measure retardance. Using this method the light intensity is modulated according to the equation

$$I_t = \frac{I_o}{2}(1 - \cos\delta) \tag{12}$$

where I_t is the transmitted intensity, I_o is the original unpolarized laser intensity before passing through the first polarizer, and δ is the total retardance of the whole flow cell. Because I_o is a constant, it is evident that the transmitted intensity is a function of just one parameter, namely the retardance, δ. However, as light passes through the flow cell, the retardance is determined by three independent quantities, namely the shear stress, τ_{rz}, and the two normal stress differences, N_1 and N_2 in the polymer and glass components. The contribution of each of these quantities to the retardance is impossible to determine from just one experimental measurement. Further ambiguity is introduced by the integration process itself, i.e., various different stress-distributions could feasibly produce the same retardance. These represent the main limitations of the current experimental set-up; similar problems have been discussed previously by Li et al. (2000) in relation to their experiments.

Table 6 Parameters fitted by least-squares to data found in literature (Schoonen 1998; Tas 1994)

Model	η_o (Pas)	λ	n	a
Carreau-Yasuda	4244	0.431	0.442	0.654

Table 7 Parameter fit to Wagner model (Tas 1994)]

Model	a	n1	n2	β
Wagner	0.92	0.21	0.07	0.06

Table 8 Maxwell modes used in simulations (Schoonen 1998)

T [°C]	G_i	λ
170	8.017×10^4	3.895×10^{-3}
	1.756×10^4	5.139×10^{-3}
	3.712×10^3	5.036×10^{-1}
	3.350×10^2	4.595×10^0

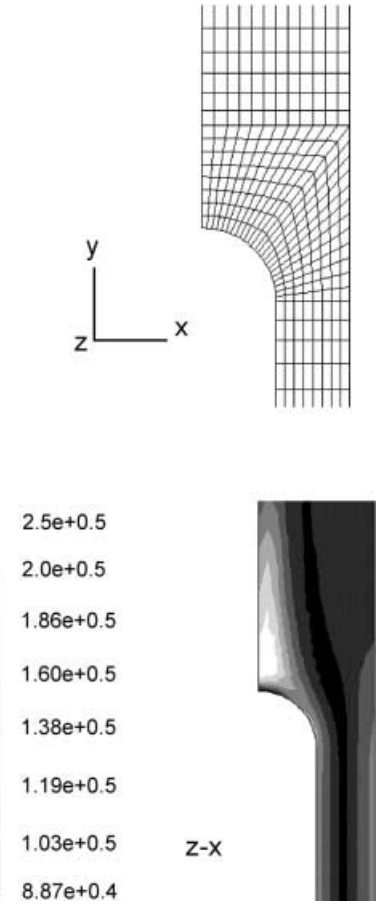

Fig. 15 The *upper diagram* shows the mesh used in the finite-element simulations. The *lower diagram* shows a gray-scale representation of the τ_{zz} component of the stress field at the highest flow rate, the scale is given in Pa

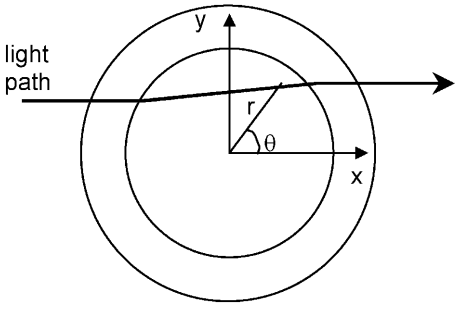

Fig. A1 Cylindrical coordinate system used in analysis of polymer melt and inner cylinder

However, some of the ambiguity in the experimental results can be removed. Examining Eqs. A14–A19, and Fig. A1 (see Appendix) we see that along the centerline ($\theta = 0$ or 180°) the polarization-state of the light is influenced solely by normal stresses. Terms containing the shear stress disappear and the birefringence is directly related to the sum of the two normal stress differences, i.e., $(N_1 + N_2 = \tau_{zz} - \tau_{\theta\theta})$. Off-centerline measurements sample both shear and normal stresses; consequently off-centerline data are more ambiguous than centerline data. However, measurements made further from the centerline pass through progressively less of the polymer. These measurements can therefore be used to estimate at what point the stress predictions in the melt begin to fail, as the light samples polymer progressively closer to the elongational region. Furthermore, the value of the off-centerline measurements in aiding visualization and verification of the results shouldn't be overlooked. For example, even if centerline predictions are significantly wrong due to errors in the rheological models' elongational stress predictions, predictions far away from the centerline should be relatively good as these are generated mainly by shear flow, which is described rather well by the constitutive model. Finally, since a given intensity can be transmitted through the set-up by a certain total retardance, but also by the same retardance plus multiples of 2π, off-centerline measurements can serve to indicate uniquely the size of the retardance along the centerline.

In Fig. 16 experimental data are represented as circles and cubic splines have been fitted to the data for visualization purposes. Comparisons with simulation results, incorporating numerically calculated stress fields, are promising and suggest the experimental

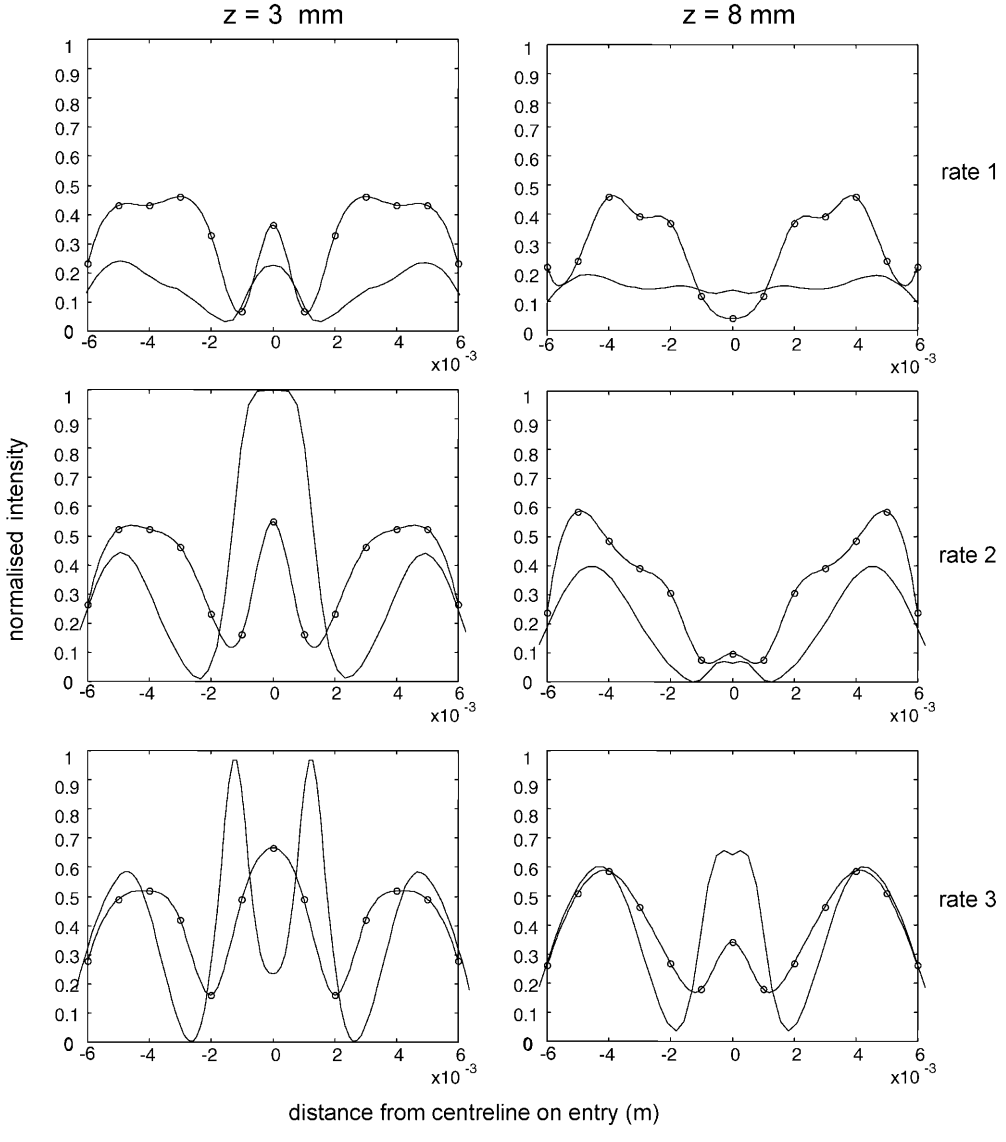

Fig. 16 Three flow-rates recorded 3 and 8 mm behind the torpedo. The experimentally produced points were measured above the centerline and reflected in the y = 0 mm line for visualization. *Continuous lines* were fitted to the experimental data using cubic splines to facilitate visualization of the results. Predictions by the optical code combined with the stress-fields calculated in finite-element simulations are plotted for comparison. The three flow-rates from top-to bottom in each figure are: 1 = 0.69, 2 = 1.04, and 3 = 1.39 $cm^3\ s^{-1}$. The corresponding Weissenberg number of each flow is: 1 = 0.91, 2 = 1.37, 3 = 1.83

method and mathematical modeling are sound. The flow rate and Weissenberg number of each experiment is given in the figure caption. The Weissenberg number definition is

$$We = \frac{\bar{\lambda} Q}{\pi R^3} \tag{13}$$

where $\bar{\lambda}$ is the mean relaxation time of the fluid, Q is the flow rate, and R is the radius of the tube. The high Weissenberg number of the flows mean that de-coupled finite element simulations had to be performed. The results are therefore only an approximation. However, the main purpose of the numerical simulations has been to verify the method and in this they are successful.

As one would expect, predictions far from the centerline tend to be better than predictions along the centerline because the shear predictions of the K-BKZ model are known to be more reliable than its elongational predictions. It appears that at low flow rates the K-BKZ model under-predicts the size of the elongational stress but as the flow rate increases the predictions quickly overtake the experimental signal and at the higher rates the size of the elongational stresses are severely over-predicted. Three distinct sources of error (the de-coupled simulation, the constitutive equation itself, and experimental error in the data) play a role in the accuracy of the comparisons of Fig. 16. While the error in the experimental data is known to be around $\pm 10\%$, at least within the region of ± 4 mm from the centerline, the error in the numerical method is unknown. Thus, at present it is difficult to evaluate properly the performance of the constitutive equation used in these simulations.

It is worth examining the relative contributions to the overall retardance of the polymer and glass components of the flow cell. Figure 17 shows a decomposition of the signal produced at the 3-mm z-position at the highest flow rate. The three distributions represent the transmitted intensity due to: the polymer birefringence alone, both the polymer and the inner glass tube, and finally the polymer and the inner tube and the outer block. The figure shows that the contribution of the inner glass tube glass is small, while that of the outer glass block is much more significant. The relative contribution of the outer block's signal will increase as the flow rate decreases. For this reason it is essential to model the thermal stresses in the outer block accurately.

In forthcoming experiments insulation will be used to decrease the size of the thermal stresses. Even so, initial tests suggest that even when the flow cell is insulated, at 170 °C, it is difficult to reduce the retardance of the outer block to less than 0.3. This is very close to the limit of 0.4 reported by Li and Burghart (1995), above which the small retardation approximation cannot be accurately employed. Thus, the option of using the low retardation approximation is not available at 170 °C. At lower temperatures, around 140 °C, one could envisage the application of this approximation, although this would entail modification of the current gear pump mechanism in order to produce very low but steady flow rates.

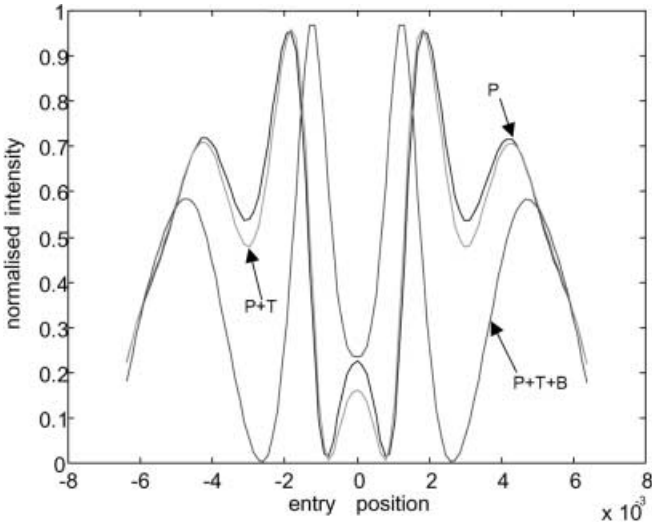

Fig. 17 Decomposition of the birefringence signal into its component parts; (P) due to polymer melt alone, (P + T) due to combined birefringence of polymer melt and glass tube, (P + T + B) due to combined birefringence of polymer melt, glass tube and the glass block

Conclusions

An axisymmetric flow cell, capable of high temperature operation, has been designed and constructed to investigate the constitutive equations of polymer melts. The main goal of the paper was to show the feasibility of the approach and the problems and solutions of such an experimental set-up. In order to interpret the results, numerous physical influences affecting the intensity of the transmitted light have been modeled. These include refraction, reflection, scattering, absorption, and birefringence. Preliminary experiments show that intensity predictions in the absence of birefringence are accurate to within approximately $\pm 10\%$ over a wide range of the flow cell. Inclusion of a numerically generated stress field shows how, in the case of high total retardation, the experiment can be used to evaluate the elongation predictions of a given rheological model. In the case of these high retardance experiments, off-centerline measurements proved useful in verifying the validity of the method and checking the reasonableness of the numerically generated stress-field. In summary, the experimental method is indeed rather complex but decades of measuring uniaxial elongational properties have provided us with a still-limited range of results in terms of extensional rates, total strain, and, more importantly,

the number of different materials studied (measurements on non-strain hardening melts using conventional techniques remains a difficult, if not impossible problem). We have high hopes that we can discern between models, especially along the center line, where the elongational properties dominate.

Appendix. Modeling reflection and birefringence

Interfaces: Fresnels' equations and the Jones vector representation

As transverse-electric, and transverse-magnetic polarized light (corresponding to vertical (V) and horizontal (H) polarization states in these experiments – Pedrotti and Pedrotti 1987) pass through a material interface, Fresnels' equations are used to predict the changes in their wave amplitudes:

$$t_v = \frac{E_t}{E} = \frac{2n\cos\theta}{n^2\cos\theta + \sqrt{n^2 - \sin^2\theta}} \tag{A1}$$

and

$$t_H = \frac{E_t}{E} = \frac{2\cos\theta}{\cos\theta + \sqrt{n^2 - \sin^2\theta}} \tag{A2}$$

We have introduced a relative refractive index $n = n_2/n_1$ where n_1 and n_2 are the refractive indices of the incident and refracting media, θ is the ray's angle of incidence, E is the amplitude of the incident electric vector, E_t is the transmitted amplitude, t is the ratio between the two, and the subscripts V and H refer to the vertical and horizontal polarization states in our lab frame.

A single ray passes through numerous interfaces before finally arriving at the screen. Thus, in order to calculate the normalized intensity reaching a given position at the screen, we must modify the amplitudes of the two components of the Jones vector, on traversing each interface. For example, C-polarized light can be expressed as

$$J = \frac{1}{\sqrt{2}}\begin{bmatrix} -i \\ 1 \end{bmatrix}$$

this Jones-vector representation containing information regarding both the amplitude and phase of the light (Hecht 1998). For circularly polarized light the component V- and H-states are of equal amplitude. The $J(1)$ component of the Jones vector corresponds to the H-component of the light, similarly the $J(2)$ component corresponds to the V-component.

Multiplying $J(1)$ by t_H and $J(2)$ by t_V gives the modified component amplitudes after the ray has traversed through an interface, i.e.,

$$J(1)_{mod} = J(1) \times t_H \tag{A3}$$

and

$$J(2)_{mod} = J(2) \times t_v \tag{A4}$$

This process is repeated at every interface. Consequently, the effect of reflection following each interface is conveniently recorded by the components of the ray's Jones vector. This approach is similar to that used in ellipsometry theory (Azzam and Bashara 1992; Fuller 1995).

The kDB-system

In isotropic media the electric, $\bar{E}$, and displacement, $\bar{D}$, vectors are related through the constitutive equation

$$\bar{D} = \varepsilon \cdot \bar{E} \tag{A5}$$

where ε is the permittivity of the medium. Furthermore, an isotropic material's refractive index is defined as

$$n = \sqrt{\frac{\varepsilon\mu}{\varepsilon_o\mu_o}} \tag{A6}$$

where μ is the materials permeability and $\sqrt{\varepsilon_o\mu_o}$ is a constant defined as the speed of light in a vacuum, c. In non-magnetic media, such as glass and polymer melts, μ is equal to one. However, the refractive index of a material under stress (i.e., anisotropic due to molecular orientation) is a second order tensor, i.e., $\underline{n}$. Thus, for non-magnetic media obeying the SOR, Eq. (A6) must be modified to account for material anisotropy, i.e.,

$$\underline{n} = \sqrt{\frac{\underline{\varepsilon}}{c}} \tag{A7}$$

Consequently, the permittivity must also be a second order tensor, i.e., $\underline{\varepsilon}$. Thus, the electromagnetic constitutive equation of a birefringent material is different to that of an isotropic material, i.e.,

$$\bar{D} = \underline{\varepsilon} \cdot \bar{E} \tag{A8}$$

Here $\bar{D}$ and $\bar{E}$ are related through $\underline{\varepsilon}$, a tensor rather than a scalar. This means that unless $\bar{E}$ happens to lie along one of the principal directions of $\underline{\varepsilon}$ then $\bar{D}$ and $\bar{E}$ are not co-linear.

By combining Maxwell's equations with the material's constitutive equation, it can be shown that for anisotropic materials two monochromatic plane waves, with two different polarizations and two different velocities, can propagate in any given direction through the material. Furthermore, in an anisotropic material it is the displacement vector, $\bar{D}$, rather than the electric vector, $\bar{E}$, that is orthogonal to $\bar{k}$, the propagation vector of the transmitted light (Born and Wolf 1964). The magnetic vector, $\bar{B}$, displacement vector, $\bar{D}$, and propagation vector, $\bar{k}$ form an orthogonal vector set that Kong (1986) refers to as the kDB system.

If one knows the direction of $\bar{k}$ then one can express the material's anisotropy in a Cartesian reference frame, in which one of the co-ordinate axes is co-linear with $\bar{D}$. For example, if this axis is chosen to be the z-axis, then $\bar{D}$ will sample material anisotropy in the xy-plane. It is for this reason that Kong (1986) and Fuller (1995) recommend calculating the material's influence on $\bar{D}$ rather than on $\bar{E}$ as light propagates through a birefringent material. To do this, the material's electromagnetic constitutive equation is used to write the electric vector in terms of the displacement vector:

$$\bar{E} = \underline{\varepsilon}^{-1} \cdot \bar{D} = \underline{\kappa} \cdot \bar{D} \tag{A9}$$

where $\underline{\kappa}$ is the impermittivity tensor and is the inverse of $\underline{\varepsilon}$. The displacement vector $\bar{D}$ thus samples the anisotropy expressed by $\underline{\kappa}$ in the plane perpendicular to $\bar{k}$.

Transforming the stress tensor to the kDB system

In the earlier section 'Component material birefringence' we discuss how the stress-field for each component in the flow cell is calculated. Here we are concerned only with the procedure of expressing the stress tensor in the kDB reference frame. Possible contributions to the change in polarization of the propagating light, due to material birefringence, come from the outer glass block, the inner glass tube and, of course, the polymer melt. The first step in the transformation procedure is to express the stresses in each of these materials in the Cartesian laboratory frame. The stresses in the outer glass block are directly calculated in the lab-frame and thus no transform is needed here. The stresses in both the inner glass tube and the polymer melt are initially calculated in cylindrical co-ordinates and require transformation to the lab-frame. The appropriate transformation equations are shown below (referring to Fig. A1).

The stresses in the inner cylinder can be expressed in the lab-frame using the following transformations:

$$\tau_{yy} = \tau_{rr}(\sin^4\theta + \cos^2\theta\sin^2\theta) + \tau_{qq}(\cos^4\theta + \cos^2\sin^2\theta) \tag{A10}$$

$$\tau_{xy} = \frac{\tau_{rr}\sin^2\theta - \tau_{\theta\theta}\cos^2\theta + \tau_{yy}(\cos^2\theta - \sin^2\theta)}{2\cos\theta\sin\theta} \tag{A11}$$

$$\tau_{xx} = \tau_{rr} + \tau_{\theta\theta} - \tau_{yy} \tag{A12}$$

$$\tau_{zz} = \tau_{xx} + \tau_{yz} = \theta \tag{A13}$$

Likewise the stresses in the polymer melt are calculated using cylindrical co-ordinates and can be expressed in the lab-frame using the following transformations:

$$\tau_{xx} = \tau_{rr}\cos^2\theta + \tau_{\theta\theta}\sin^2\theta \tag{A14}$$

$$\tau_{yy} = \tau_{rr}\sin^2\theta + \tau_{\theta\theta}\cos^2\theta \tag{A15}$$

$$\tau_{zz} = \tau_{zz} \tag{A16}$$

$$\tau_{xy} = (\tau_{rr} + \tau_{\theta\theta})\cos\theta\sin\theta \tag{A17}$$

$$\tau_{xz} = \tau_{rz}\cos\theta \tag{A18}$$

$$\tau_{yz} = \tau_{rz}\sin\theta \tag{A19}$$

where the z-axis corresponds to the long axis of the flow cell and the angle θ is taken from the positive x-axis.

The propagation angle, α, that $\bar{k}$ makes with the laboratory's x-axis on entering each material is given by trigonometrical calculation and Snell's law. Because in our experiments $\bar{k}$ is refracted either upwards or downwards, but always remains in the laboratory's xy-plane, a simple 2-D rotation matrix can be used to express the stress-tensor, $\underline{\tau}$, in a frame with its new x-axis, or x'-axis, co-linear with $\bar{k}$ the propagation-vector, i.e.,

$$\underline{\tau}' = \underline{R}^{-1} \cdot \underline{\tau} \cdot \underline{R} \tag{A20}$$

where $'$ denotes the tensor expressed in the rotated frame and

$$\underline{R} = \begin{bmatrix} \cos(\alpha) & \sin(\alpha) & 0 \\ -\sin(\alpha) & \cos(\alpha) & 0 \\ 0 & 0 & 1 \end{bmatrix} \tag{A21}$$

The rotation of the reference frame is represented in Fig. A2.

Thus, given $\underline{\tau}'$ we can calculate $\underline{n}$ using Eq. (1), Eq. (A7) gives $\underline{\varepsilon}'$, and $\underline{\kappa}'$ is just the inverse of $\underline{\varepsilon}'$.

Birefringence calculation

Using the above procedure we obtain $\underline{\kappa}$, the impermittivity expressed in a co-ordinate frame in which one of the co-ordinate axis is co-linear with $\bar{k}$. As mentioned previously, $\bar{D}$ samples the material anisotropy in the plane orthogonal to $\bar{k}$. This means that the material anisotropy sampled by $\bar{D}$ is expressed by a 2×2 sub-matrix of $\underline{\kappa}'$. For example, if $\underline{\kappa}'$ is written as

$$\underline{\kappa}' = \begin{bmatrix} \kappa_{x'x'} & \kappa_{x'y'} & \kappa_{x'z'} \\ \kappa_{y'x'} & \kappa_{y'y'} & \kappa_{y'z'} \\ \kappa_{z'x'} & \kappa_{z'y'} & \kappa_{z'z'} \end{bmatrix} \tag{A22}$$

and if $\overline{\overline{\omega}}\bar{k}$ is directed along the z'-axis of the rotated frame, then the 2×2 sub-matrix sampled by $\bar{D}$ is

$${}^{*}\underline{\kappa}' = \begin{bmatrix} \kappa_{x'x'} & \kappa_{x'y'} \\ \kappa_{y'x'} & \kappa_{y'y'} \end{bmatrix} \tag{A23}$$

This sub-matrix can be drawn geometrically as an ellipse lying in the DB-plane. Born and Wolf (1964) show that the two linearly polarized $\bar{D}$ vectors that propagate simultaneously through the anisotropic material vibrate perpendicular to each other, and that their directions of vibration coincide with the principal semi-axis of the ${}^{*}\underline{\kappa}'$ ellipse. Thus, if we first determine the eigenvalues of ${}^{*}\underline{\kappa}'$ (the lengths of the two principal semi-axes), along with the orientation angle of its principal axis, we can subsequently find the principal values of the refractive index tensor in this plane. These are calculated as

$$n_{+,-}^2 = \frac{1}{c^{2*}\kappa'_{+,-}} \tag{A24}$$

where the $_+$ and $_-$ subscripts represent the two eigenvalues of the ellipse. The birefringence of the material measured in the kDB frame is then

$$\Delta n = n_+ - n_- \tag{A25}$$

The eigenvectors of the ellipse give the orientation angle, χ, of the principal axis.

Jones calculus

The stresses and therefore the optical properties of the materials in the flow cell change continuously along the path length of each light ray. Two alternative methods can be applied to account for a birefringent material's influence on the polarization-state of propagating light, Jones and Mueller calculus. The influence of partial-reflection at the interfaces in the experiment, is best recorded using the Jones vector representation (see the above section 'Interfaces: Fresnels' equations and the Jones vector representation'). Thus, Jones (Jones 1941, 1948) rather than Mueller calculus subsequently provides a more natural choice to calculate birefringence effects.

The treatment involves discretizing the path of the rays into individual elements. Each element is considered to have constant optical properties. The analysis is fully explained by Azzam and Bashara (1992) and Fuller (1995) in which the Jones matrix of a birefringent element oriented at χ is given as

$$M = \begin{bmatrix} \cos\delta/2 + i.\cos 2\chi.\sin\delta/2 & i.\sin 2\chi.\sin\delta/2 \\ i.\sin 2\chi.\sin\delta/2 & \cos\delta/2 - i\cos 2\chi.\sin\delta/2 \end{bmatrix} \tag{A26}$$

where $\delta = \{2\pi(\Delta n).d\}/\lambda$ is the retardance and χ is the orientation angle of the ellipse.

The Jones matrix for a given light ray propagating through a stressed component of the flow cell is found by multiplying together all the Jones matrices of the discretized elements, along its entire path in the material, e.g.,

$$M_{polymer} = M_1 \cdot M_2 \cdot M_3 \cdot \ldots\ldots \cdot M_i \tag{A27}$$

where the subscript indicates the element number of the discretized polymer core. In this way we find the Jones matrix of a particular flow cell component, along a given ray path.

Determination of intensity at screen

The intensity, propagated in each component of the Jones vector, is proportional to the square of its amplitude. Thus

$$P_H \propto J_{mod}(1) \times J^*_{mod}(1) \tag{A28}$$

and

$$P_V \propto J_{mod}(2) \times J^*_{mod}(2) \tag{A29}$$

where the * indicates the complex conjugate. (The proportionality constant between power and amplitude depends on the propagation direction and refractive index ratio between the materials on either side of the interface.) Furthermore, the total intensity of the ray is proportional to the sum of the intensities in these two components:

$$total\ intensity \propto P_T = P_H + P_V \tag{A30}$$

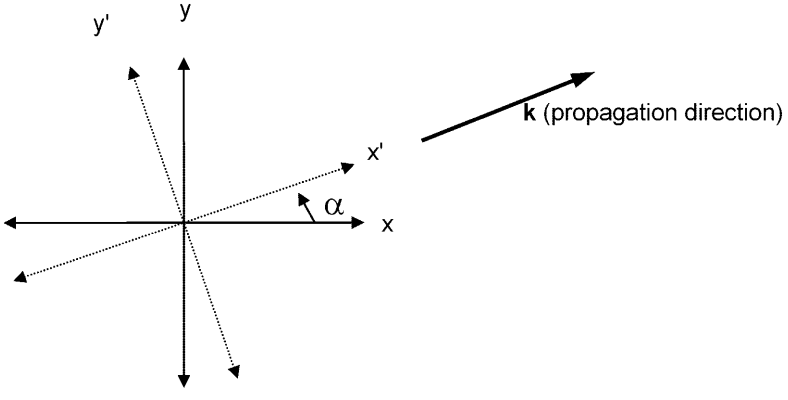

Fig. A2 Given the propagation angle, α, a rotation matrix can be used to express the stress-tensor in this rotated frame

Note that in Eqs. (A1) and (A2), t can be greater than 1, i.e., the amplitude can increase on traversing an interface. This is possible because of changes in the cross-section and speed of the wave. For this reason the intensity distribution propagating within a material must be normalized with respect to the maximum intensity that could be transmitted *in that same material*. The maximum possible intensity that can be transmitted through the flow cell, in the absence of birefringence, is along the centerline. If this is defined in a given material as $P_{Tcenterline}$, then the normalized transmitted intensity of a ray, following an arbitrary path through the flow cell is

$$normalized\ transmitted\ intensity = P_T/P_{Tcenterline} \quad \text{(A31)}$$

Thus the Jones-vector of each ray in the Perspex screen is calculated and normalized with respect to the maximum intensity that could be transmitted along the centerline in the Perspex screen.

Summary of calculation

Using the methods outlined in this Appendix, the final Jones-vector, and consequently the normalized intensity, of a ray propagating through the entire optical set-up can be determined. The procedure is summarized as follows:

- The modified Jones-vector of a light ray after passing through an interface is determined (the first section of this Appendix).
- If the next material component through which the ray propagates is birefringent, then the component's Jones-matrix is determined and multiplied with the rays (modified) Jones-vector. This simulates the propagation of the ray in the birefringent material (the second, third, fourth, and fifth sections of this Appendix).
- This modification procedure continues through all interface and material components until the ray reaches the translucent screen. The final Jones vector arriving at the screen can be used to calculate the normalized intensity distribution due to reflection and material anisotropy (the sixth section of this Appendix).
- The normalized intensity distribution due to reflection and material anisotropy is multiplied by the distributions due to spreading, scattering, and absorption. The result is the final intensity arriving at the translucent screen due to all effects.

References

Azzam RMA, Bashara NM (1992) Ellipsometry and polarized light. Elsevier Science Publishers B.V.

Baaijens FTP, Baaijens JPW, Peters GWM, Meijer HEH (1994) A numerical and experimental investigation of viscoelastic flow around a cylinder. J Rheol 38:351–376

Baaijens JPW, Peters GWM, Baaijens FPT, Meijer HEH (1995) Viscoelastic flow past a confined cylinder of a polyisobutylene solution. J Rheol 39:1243–1277

Bernstein B, Kearsley EA, Zapa LJ (1963) A study of stress relaxation with finite strain. Trans Soc Rheol 7:391–410

Bogaerds ACB, Verbeeten WMH, Peters GWM, Baaijens FPT (1999) 3D Viscoelastic analysis of a polymer solution in a complex flow. Computat Methods Appl Mech Eng 180:413–430

Born MA, Wolf E (1964) Principles of optics. Electromagnetic theory of propagation, interference and diffraction of light, 2nd edn. Pergamon Press

Callister WD (1997) Materials science and engineering: an introduction, 4th edn. Wiley

Cengel YA, Boles MA (1994) Thermodynamics. An engineering approach, 2nd edn. McGraw-Hill

Debae F, Legat V, Crochet MJ (1994) Practical evaluation of four mixed finite element methods for viscoelastic flow. J Rheol 38(2):421–442

Douven LFA, Baaijens FPT, Meijer HEH (1995) The computation of properties of injection-moulded products. Prog Polym Sci 20:403–457

Fuller GG (1995) Optical rheometry of complex fluids. Oxford University Press, New York

Galante SR, Frattini PL (1991) The influence of end effects on birefringence measurements in nominally two-dimensional channel flows. J Rheol 38(8):1551–1581

Harrison P (2000) Rheo-optics software for heated axisymmetric stagnation flowcell. Technical Report MT 00.016, Eindhoven University of Technology

Hecht E (1998) Optics, 3rd edn. Addison Wesley Longman, Amsterdam

Janeschitz-Kriegl H (1983) Polymer melt rheology and flow birefringence. Springer, Berlin Heidelberg New York

Janssen LJP (2000) Development of an axisymmetric stagnation flowcell for measuring FIB in polymer melts. Eindhoven University of Technology (W/Mate) Technical Report MT 00.017

Jones RC (1941) J Opt Soc Am 31:488

Jones RC (1948) J Opt Soc Am 38:671

Kaye A (1962) Non-Newtonian flow in incompressible fluids. Part I: A general rheological equation of state. Part II. Technical Report Note No. 134, College of Aeronautics, Cranfield, UK

Kong J-A (1986) Electromagnetic waves, 4th edn. Wiley

Kroger M, Luap C, Muller R (1997) Polymer melts under uniaxial elongational flow: stress-optical behaviour from experiments and nonequilibrium molecular dynamics computer simulations. Macromolecules 30:526–539

Li J-M, Burghardt WR (1995) Flow birefringence in axisymmetric geometries. J Rheol 39:743–766

Li J-M, Burghardt WR, Yang B, Khomami B (1998) Flow birefringence and computational studies of a shear thinning polymer solution in axisymmetric stagnation flow. J Non-Newtonian Fluid Mech 74:151–193

Li J-M, Burghardt WR, Yang B, Khomami B (1999) Uniaxial extension characterization of a shear thinning fluid using axisymmetric flow birefringence. J Rheol 43:147–165

Li J-M, Burghart WR, Yang B, Khomami B (2000) Birefringence and computational studies of a polystyrene Boger fluid in axisymmetric stagnation flow. J Non-Newtonian Fluid Mech 91:189–220

Lodge AS (1955) Variation of flow birefringence with stress. Nature 176:838–839

McLeish TCB, Larson RG (1998) Molecular constitutive equations for a class of branched polymers: the Pom-Pom polymer. J Rheol 42(1):81–110

Pedrotti FL, Pedrotti LS (1987) Introduction to optics. Prentice-Hall, New Jersey

Peters GWM, Schoonen JFM, Baaijens FPT, Meijer HEH (1999) On the performance of enhanced constitutive models for polymer melts in a cross-slot flow. J Non-Newtonian Fluid Mech 82:387–427

Schoonen JFM (1998) Determination of rheological constitutive equations using complex flows. PhD thesis, Eindhoven University of Technology, The Netherlands

Schoonen JFM, Swartjes FHM, Peters GWM, Baaijens FTP, Meijer HEH (1998) A 3D numerical/experimental study on a stagnation flow of polyisobutylene solution. J Non-Newtonian Fluid Mech 79:529–561

Schott (1998) Schott Optisches Glas. Taschenkatalog

Tas P (1994) Film blowing: from polymer to product. PhD thesis, Eindhoven University of Technology, The Netherlands

Ugural AC, Fenster SK (1995) Advanced strength and applied elasticity, 3rd edn. Prentice-Hall

Verbeeten WMH, Peters GWM, Baaijens FPT (2001) Differential constitutive equations for polymer melts: the enhanced pom-pom models. J Rheol 45(4):823–843

Wagner MH (1976) Das Folienblasverfahren als rheologische-thermodynamische prozess. Rheol Acta 15:40–51

Wagner MH (1977) Rheol Acta 16:43

Wagner MH, Raible T, Meissner J (1979) Rheol Acta 18:427